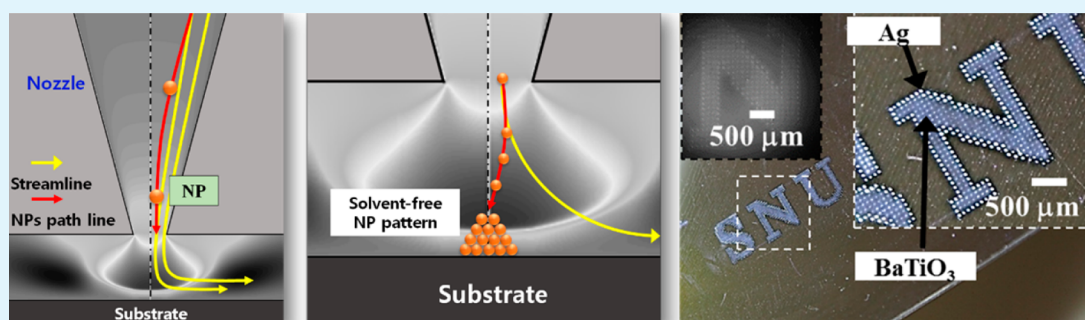# Aerodynamically Focused Nanoparticle (AFN) Printing: Novel Direct Printing Technique of Solvent-Free and Inorganic Nanoparticles

Gil-Yong Lee,[†] Jae-Il Park,[†] Chung-Soo Kim,[†] Hae-Sung Yoon,[†] Jinkyu Yang,[#] and Sung-Hoon Ahn*,[†,‡]

[†]Department of Mechanical and Aerospace Engineering and [‡]Institute of Advanced Machinery and Design (IAMD), Seoul National University (SNU), Seoul 151-742, Republic of Korea
[#]William E. Boeing Department of Aeronautics & Astronautics, University of Washington, Seattle, Washington 98195, United States

S *Supporting Information*

ABSTRACT: Aerodynamically focused nanoparticle (AFN) printing was demonstrated for direct patterning of the solvent-free and inorganic nanoparticles. The fast excitation-purge control technique was proposed and investigated by examining the aerodynamic focusing of nanoparticles and their time-scale, with the analytical and experimental approaches. A series of direct patterning examples were demonstrated with Barium Titanate (BaTiO$_3$) and Silver (Ag) nanoparticles onto the flexible and inflexible substrates using the AFN printing system. The capacitor and flexible conductive line pattern were fabricated as the application examples of the proposed technique. The results presented here should contribute to the nanoparticle manipulation, patterning, and their applications, which are intensely being studied nowadays.

KEYWORDS: aerodynamic focusing, solvent-free nanoparticle, direct printing, time-scaling

Nanoparticle (NP) manipulation is essential for many scientific and engineering applications.[1−3] Especially, because of its flexibility and compatibility, localized NP patterning has been a subject of intense study, with promising new developments in microelectronics,[4−9] energy devices,[10] and optics.[11] Although inkjet printing is the most representative patterning technique for dispensing NPs with a solvent,[5,9] it is more challenging to pattern solvent-free NPs directly to the designed position.[2,7,12] Moreover, regarding the recent growing role of inorganic NPs (e.g., metal oxides, gold, or silver) in energy, biotechnology, and nanotechnology,[10,13] solvent-free NP printing offers potential advantages.[1,2,14,15] Recent efforts have presented the patterning of inorganic and solvent-free NPs from the nanoscale to the mesoscale. For example, ion-induced focusing of charged NPs and their patterning have been introduced.[1,2] Traditionally, the cold spray (CS) method,[6,16] aerosol deposition method (ADM),[15] and nanoparticle deposition system (NPDS)[14] have been used for metal oxide or metal NP deposition. However, these methods concerned the high-speed impact of NPs on the substrates, without considering the focusing effect. Several recent studies have investigated microscale pattern formation with aerodynamically focused NPs. Silver and copper NPs were deposited in a conductive line at the submillimeter scale.[6,17] Other studies

have shown the focusing of NPs using an aerodynamic lens.[18−20] Aerosol jet printing deposits atomized ink aerosols onto the substrate focused by a sheath gas.[8,21] The aerodynamic focusing of NPs has a straightforward working principle, and is superior to solvent-based processes involving patterning inorganic and uncharged NPs at room temperature; however, few studies have addressed precise direct patterning of NPs.

Here, we present a novel direct printing technique for solvent-free and inorganic NPs, referred to as aerodynamically focused nanoparticle (AFN) printing, based on the principle of aerodynamic focusing. By introducing the time-scaling of NPs via fast control of excitation and purging, we were able to direct the high-speed and focused NP beam for patterning. The aerodynamic focusing mechanism was used to define the optimized NP time-scale (relaxation time, τ)[22,23] with respect to the source pressure of the gas and the NP diameter. We observed that time-scaling helps to direct only the small NPs whose diameters are in the optimum region, by terminating the excitation before larger NPs can respond to the gas. Figure 1a−
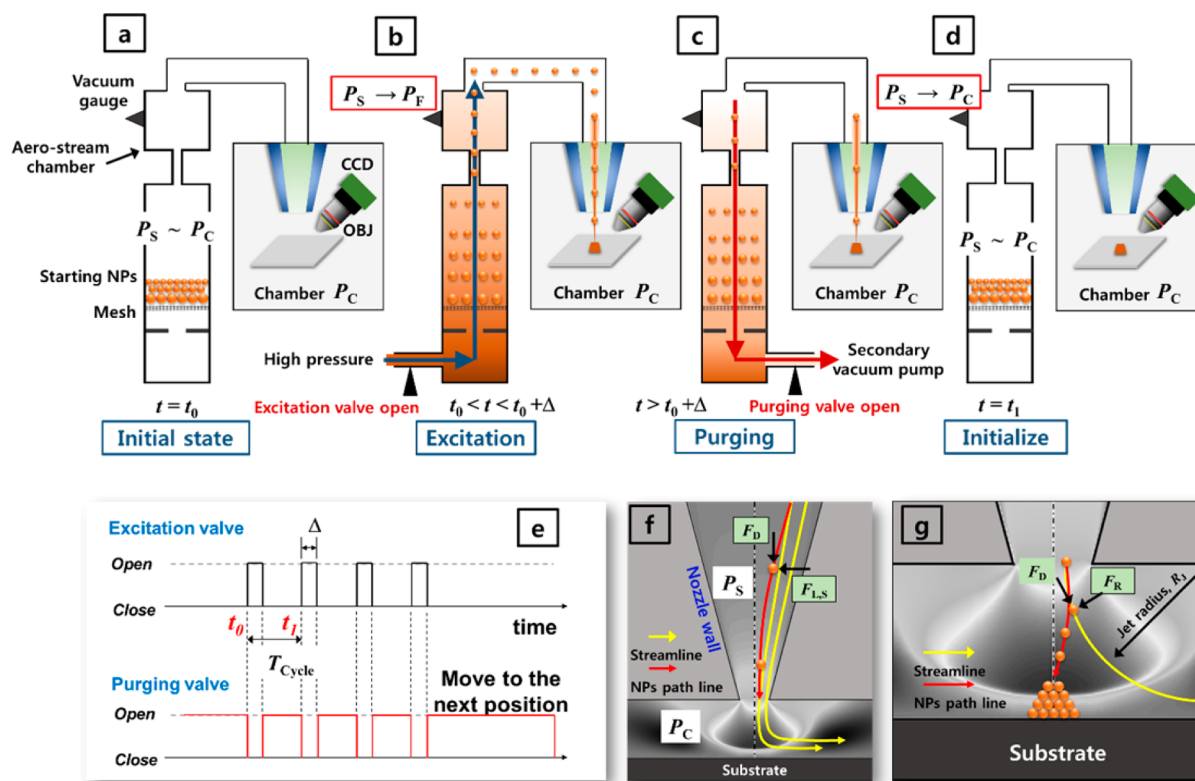
Figure 1. (a−d) Schematic diagram of the processing steps and (e) timing diagram of the AFN printing. (f−g) Nozzle flow induced by the high pressure difference depicting the NP path line; the drag and inertia forces exerted on the NPs. The gas flow field was calculated from CFD simulations. The flow field is gray-scaled in this figure to depict the particle motion clearly.

d shows a schematic diagram of the proposed system. The timing diagram is shown in Figure 1e. In the Supporting Information, S-1 and S-2, we describe the entire process in detail with movie clip (see the Supporting Information, Movie 1). The incident opening of the excitation valve at $t = t_0$ disperses the starting NPs into the induced gas stream (see the Supporting Information, S-3) and creates an instant pressure increase inside the aero-stream chamber which acts as the source pressure, P_S, inducing the nozzle flow (Figure 1b). The increased source pressure results in a decrease in the NPs' time-scale, resulting in their rapid adjustment to the induced gas flow.[18,22,23] The excitation lasts for time duration Δ. After the termination of the excitation process, purging is initiated (Figure 1c) by decreasing the source pressure before exceeding the optimum pressure P_F, where NPs are routed into a high-velocity focused beam. At $t = t_1$ ($t_0 + T_{Cycle}$), after the source pressure is reset to low pressure (Figure 1d), the next excitation and purging cycle is initiated. After repeating the cycle N times, the routing position is moved to the next position using a translation stage. The pulsed excitation-purge mechanism helps to prevent nozzle clogging and excessive airborne NPs near the substrate by minimizing the amount of NPs routed through the nozzle (see the Supporting Information, S-4) and to maintain the low pumping capacity of the vacuum system to reduce the system costs. Additionally, this pulsed routing enables digital patterning, similar to the drop-on-demand (DOD) ink dispersion system used in most inkjet printing, with addressing a potential advantage over the conventional aerosol based printing techniques which use the continuous carrier gas (e.g., CS, ADM, NPDS, and aerosol jet printing). In this study, we used the proposed AFN printing technique to demonstrate

patterning examples of the metal oxide (BaTiO$_3$) NPs, widely used as a dielectric material for a capacitor and a lead-free piezoelectric material[24,25] as well as the metal (Ag) NPs as a conductive pattern[4,8] on various substrates, including flexible and transparent substrates, having a pattern resolution on the order of 10 μm. The capacitor and flexible conductive line pattern were fabricated by the proposed technique to show the capabilities of the AFN printing for the device fabrication.

To choose proper process conditions, we first defined the optimum process region to create a focused beam of NPs, having the maximum impact velocity. Computational fluid dynamics (CFD) simulations were conducted to verify our analytical approach. Explanations of the determination of the excitation−purge time-scale Δ and T_{Cycle} are given with the experiments. Figure 1f, g shows a schematic diagram of NPs routed through a nozzle, separated from the streamline, and directed to a position on the substrate for pattern formation. To accelerate the NPs to a high velocity, a high pressure ratio (>100) is created between the upstream gases (source pressure, P_S) and downstream gases (chamber pressure, P_C) in the nozzle.[14,15,17,26] Stokes' drag law for small particles having a small-particle Reynolds number was used to determine the drag force F_D on the NPs.[18,23] In the upstream region, Saffman's lift force $F_{L,S}$ acts as an inertial effect pushing the NPs to where the gas velocity is higher,[6,27] usually in the direction of the flow axis. Thus, the NPs' radial position shifts to the axis separated from the streamline (Figure 1f). In the downstream region, the curvilinear motion of the streamline, due to the substrate, creates a centrifugal force F_R as an inertial effect (Figure 1g).[18,19,23] To accelerate NPs to a maximum speed, a large drag force is preferable. The relative magnitudes of these three forces
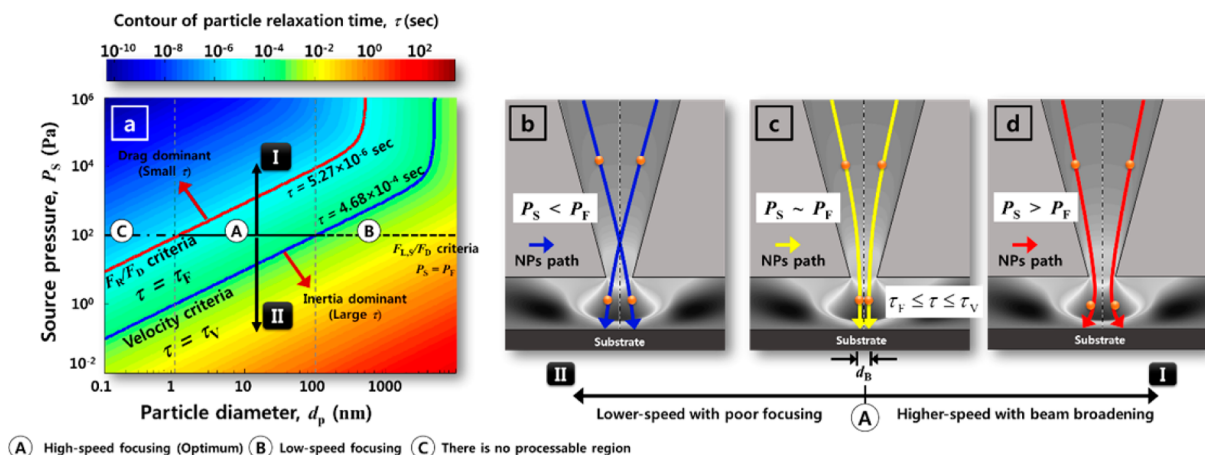
Figure 2. (a) Contour plot of the NPs' time-scale (relaxation time, τ) with the source pressure, P_S, and NP diameter, d_p. Here, we used BaTiO$_3$ NPs, with $P_F = 109$ Pa, $\tau_F = 5.27 \times 10^{-6}$ s, and $\tau_V = 4.68 \times 10^{-4}$ s, calculated in the Supporting Information (S-5). (b) NPs routed with low impact velocity and poor focusing when $P_S < P_F$. (c) In the optimum region, NPs were routed with a focused beam and high impact velocity. (d) As the source pressure P_S increased further, the NPs accelerated to a considerably greater velocity, resulting in beam broadening.
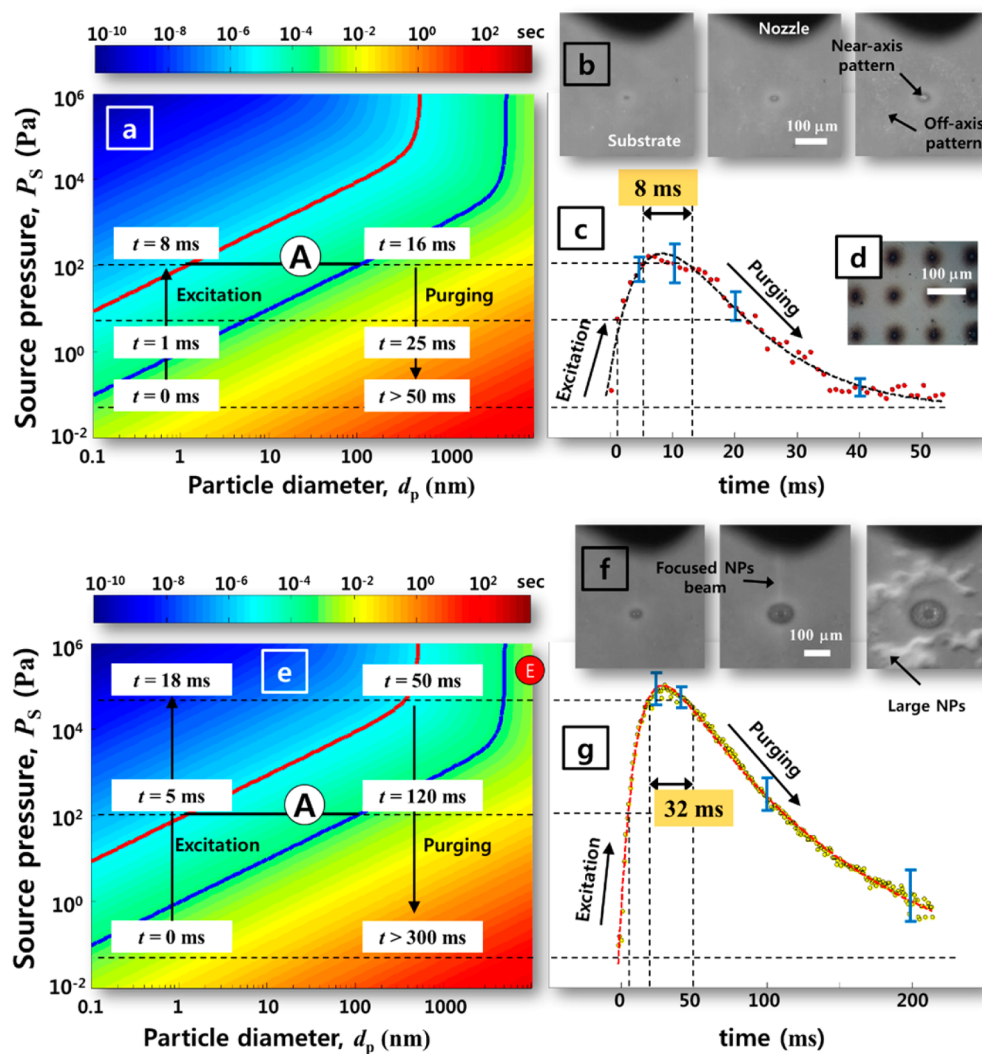

Figure 3. Time history of the source pressure P_S, measured during the excitation–purge sequence on the contour plot of the NPs' time-scale when (a) $\Delta = 10$ ms and (e) $\Delta = 40$ ms. In situ images taken with the CCD camera during the excitation and purging when (b) $\Delta = 10$ ms and (f) $\Delta = 40$ ms (BaTiO$_3$ NPs were patterned, and a Si substrate was used). Measured average source pressure P_S (for five cycles of excitation and purging) when (c) $\Delta = 10$ ms and (g) $\Delta = 40$ ms with their curve fittings. (d) Representative point patterns of BaTiO$_3$ NPs printed by setting $\Delta = 10$ ms, $T_{Cycle} = 100$ ms, and $N = 1$.
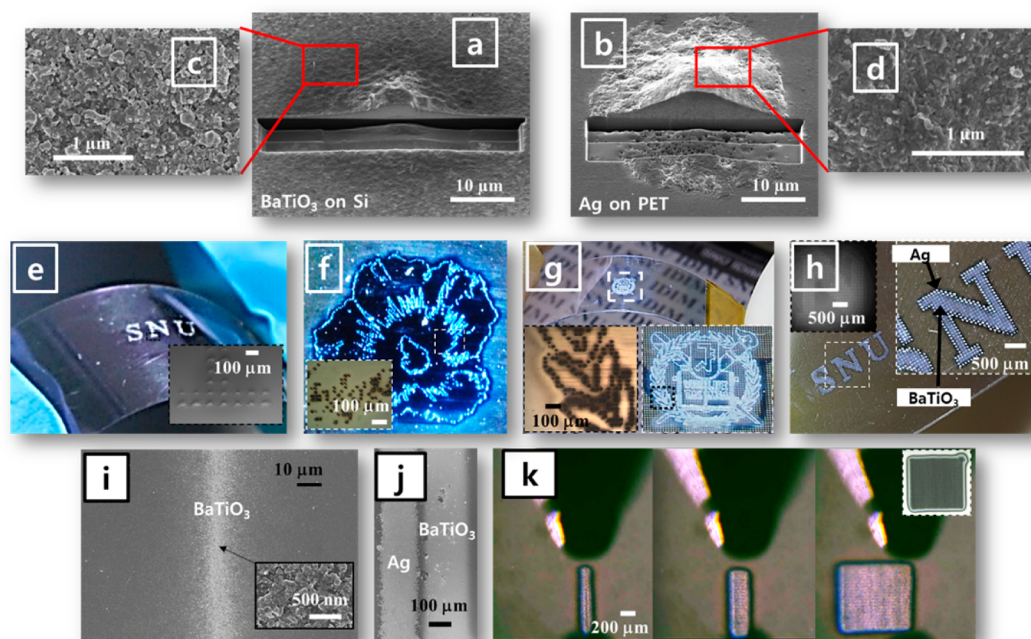
Figure 4. Scanning ion microscopy (SIM) image of (a) a BaTiO$_3$ NPs point pattern on a Si substrate and (b) a Ag NPs point pattern on a PET substrate (Δ = 10 ms, T_{Cycle} = 100 ms, and N = 3). To observe the cross-section, a focused ion beam was used for machining, and SIM images were taken with a tilt angle of 30° after machining. (c, d) Magnified scanning electron microscopy (SEM) images showing the surface morphology of the patterns. The patterns consisted of NPs of diameters 10−100 nm. (e) Ag NPs patterned on a PET substrate with a pattern resolution of 100 μm. 400 point patterns of Ag NPs, consisting of the letters "SNU", printed by setting Δ = 10 ms, T_{Cycle} = 100 ms, and N = 3. (f) 2000 point patterns of BaTiO$_3$ NPs on a Si substrate (Δ = 10 ms, T_{Cycle} = 200 ms, and N = 2) to depict "Sharon's Rose" (the Korean National Flower). (g) 4000 point patterns of BaTiO$_3$ NPs on a PET substrate (Δ = 10 ms, T_{Cycle} = 200 ms, and N = 2) to construct the emblem of Seoul National University (SNU). A 30 μm pattern resolution was used for these examples. (h) 200 point patterns of Ag NPs (boundary of patterns) and 300 point patterns of BaTiO$_3$ NPs (interior of the patterns) printed on a PET substrate with a pattern resolution of 100 μm (Δ = 10 ms, T_{Cycle} = 100 ms, and N = 2). (i, j) Line patterns of BaTiO$_3$ and Ag NPs on Si substrates. (k) Rectangular pattern of BaTiO$_3$ on a Cu-coated (sputter deposition) Si substrate. In the Supporting Information, S-12, optical microscopy and surface profile measurement data for the rectangular pattern are provided.

(F_D, $F_{L,S}$, and F_R) play a major role in manipulating NPs to a small divergence to form a focused NP beam with diameter d_B. In the Supporting Information, S-5, we provide the detail calculations of the optimum process window with respect to the optimum source pressure, P_F and time-scale of NPs, τ_F and τ_V. Figure 2a shows a contour plot of the NPs' time-scale τ, with respect to the NP diameter d_p and source pressure P_S. After defining the boundaries of the optimum region (i.e., P_F, τ_F, and τ_V, calculated in the Supporting Information, S-5) on this contour, one can determine the optimum processing pressure for the given NP diameter range. In this example, NPs ranging from 1 to 100 nm in diameter were focused to a narrow beam having the maximum positioning velocity, by maintaining P_S at 109 Pa (Figure 2a, Line A), whereas larger NPs (>100 nm) were focused, but their speed at positioning was lower, compared with that of the smaller NPs, for P_S = 109 Pa (Figure 2a, Line B). A similar conclusion was reached for NPs <1 nm in size; in this case, the smaller-sized NPs accelerated much faster, however, the NP beam was broader (Figure 2a, Line C). If the pressure increased from Line A, then the particle time-scale decreased, resulting in the higher positioning velocity and NP beam broadening (Figure 2a, in the direction of I). However, poor focusing was observed when the pressure decreased from Line A in the direction of II (Figure 2a). In Figure 2b−d, the path lines of the NPs are shown for the different regions of P_S and τ. The CFD simulations with NP trajectories and velocities, presented in the Supporting Information, S-6, were in good agreement with the results

described above. For example, when P_S was 70 Pa, 100 nm BaTiO$_3$ NPs were focused to a beam diameter d_B of ~12 μm onto the substrate, having a maximum positioning velocity of 61.5 m s^{-1}.

To determine the proper value of Δ to accelerate NPs in the optimum region, we considered the velocity of NPs accelerated by the drag force for Δ, expressed as $u_p = u_g(1 - e^{-\Delta/\tau})$.[23] Here, Δ should be sufficiently long for NP acceleration in the optimum diameter region, but short enough to prevent larger NPs from responding to the gas. In the Supporting Information, S-7 (Figure S5), we present an example of normalized NP velocity with varying Δ, when P_S = 109 Pa. In this example, by setting Δ to 1×10^{-2} s (10 ms), NPs ranging from 1 to 100 nm were accelerated to their terminal velocity, while NPs larger than 1 μm were not. Thus, Δ can be customized to the appropriate value by considering the time-scale of the target NPs. As we described in the introductory part, this provides the way to excite the small NPs (i.e., we can excite only the desired NPs whose diameters are in the excitation band) separating them from larger or aggregated NPs in a solvent-free environment.

Figure 3a−d shows the time history of the source pressure P_S measured in the experimental setup shown in Figure 1a−d with the in situ images taken inside the chamber. The source pressure increased (decreased) exponentially with excitation (purging). Here, when we set Δ to 10 ms, consistent with the above results, the average P_S crossed the optimum value P_F (109 Pa) in 8 ms; the maximum average P_S reached nearly 150

Pa at $t \sim 10$ ms. By initiating purging after 10 ms, P_S decreased to its initial pressure P_C (~ 0.1 Pa) at $t \sim 50$ ms. Because the next excitation should be activated after P_S is initialized to P_C, T_{Cycle} should be larger than 50 ms (we took T_{Cycle} as 100 ms for the following patterning examples). Considering that the printing speed is directly related to Δ and T_{Cycle}, it is also worthwhile to examine the way to decrease Δ and T_{Cycle} for the improvement of the printing speed with its limitation. We provide further discussion in the Supporting Information, S-8. Figure 3b shows the microscale pattern printed by the focused NPs, and their subsequent high-speed impact on the substrate during the excitation (see the Supporting Information, S-9 and the movies). It should be noted that the NPs were focused within 50 μm through the 500-μm nozzle opening, which is $\sim 10\times$ larger than the pattern diameter. Also, we observed unexpected routings of NPs that created an off-axis pattern, which would give a diffused interface for large area patterning applications. However, this off-axis pattern can be removed by sonication (for ~ 10 s) without affecting the main near-axis pattern. See further discussions for the near-axis and off-axis pattern in the Supporting Information, S-10. With successful excitation and purging cycles, NP patterns could be printed at a designed position. In Figure 3d, representative point patterns of BaTiO$_3$ NPs are shown.

Figure 3e–g presents a more extreme situation when NPs were excited over a longer time period Δ; as expected, the main problem in this case is that P_S increased significantly beyond the optimum region (much more in the direction of I in Figure 2a), which resulted in beam broadening with very high-speed routing of NPs during excitation. It is worthwhile to examine this, because the high-speed positioning of NPs can be observed more clearly for a reduced time-scale τ, over the entire NP diameter range. Under excitation, small NPs were first routed into a narrowly focused beam (first image of Figure 3f). Over time, a highly focused beam of large NPs developed (second image of Figure 3f). Because the excitation period Δ was sufficient to accelerate the larger NPs, the excitation band extended to the 10-μm diameter NPs, causing their uncontrolled routing, as shown in the third image of Figure 3f. NPs whose diameters were greater than 10 μm were located in a lower region than the $\tau = \tau_V$ boundary; thus, these NPs were not directed in a desirable way (region marked as red-filled circle E in Figure 3e).

Taking the novelties of the proposed AFN printing technique, we present a series of direct patterning examples of functional, solvent-free NPs onto inflexible and flexible substrates, with ~ 10 μm resolution (the maximum resolution observed). In Figure 4a–d, scanning ion microscopy (SIM) and scanning electron microscopy (SEM) images of the representative point patterns of BaTiO$_3$ and Ag NPs are shown. Figure 4a, b shows that the widths of the BaTiO$_3$- and Ag-NP patterns were ~ 40 and 35 μm, respectively. To see the cross-section, we machined each deposition using a focused ion beam (FIB). Magnified SEM images (Figure 4c, d) showed that the patterned surface consisted of NPs ranging in diameter from 10 to 100 nm, (i.e., no evidence of NPs having a diameter >1 μm in the pattern). SEM images of the initial NPs (see the Supporting Information, S-11) show their broad diameter distributions (from 10 nm to 1 μm for BaTiO$_3$ NPs) and their aggregated form, however, we directed the NPs for pattern formation for the designed NPs only by the suggested excitation-purge mechanism (time-scaling). Moreover, densely patterned microstructures were possible, implying that the NPs

retained their high kinetic energy during impact with the substrates. High-resolution, dense NP patterns were fabricated at room temperature in a solvent-free environment, using the AFN printing without thermal treatment. In Figure 4e–k, more challenging pattern examples are presented. Ag NPs were patterned onto a flexible-transparent polyethylene terephthalate (PET) substrate having a pattern resolution of 100 μm (Figure 4e). BaTiO$_3$ NPs were patterned onto a Si substrate (Figure 4f) and a PET substrate (Figure 4g) with 30-μm pattern resolution. To show the multimaterial patterning capability, we present Ag and BaTiO$_3$ NPs patterned onto a PET substrate, with a pattern resolution of 100 μm (Figure 4h). BaTiO$_3$ and Ag NPs can be patterned onto a Si substrate with narrow line patterns by moving the substrates during excitation and purging cycles (Figure 4i, j). In Figure 4i, it should be noted that metal oxide (BaTiO$_3$) NPs can be directly printed within a 10-μm width, which has not been realized in existing solvent-free and aerodynamic printing techniques; a rectangular pattern was also printed (Figure 4k). The selected movie clips captured the real-time patterning of Figure 4f–h and k in the Supporting Information, S-2 (Movie 1). To show the capabilities of the AFN printing for the device fabrication, we also showed the application examples in the Supporting Information, S-12 (the capacitor and flexible conductive line pattern) with the test results (see the Supporting Information, S-12)

In summary, aerodynamically focused nanoparticle (AFN) printing was demonstrated for direct patterning of the solvent-free and inorganic NPs. The fast excitation-purge control technique was proposed with examining the aerodynamic focusing of NPs and their time-scale, presenting the feasibility and reliability of the proposed method with the analytical and experimental approaches. The important advantages of the AFN printing are (i) it is a simple and cost-effective technique to direct high-speed focused NP beam to form a high-resolution pattern; (ii) the NPs can be routed on-demand requirements, similar to the DOD printing capability of inkjet; (iii) the NPs can be patterned at room temperature in a solvent-free environment; and (iv) various types of NPs (e.g., oxides and metals) can be printed on a flexible substrate, as well as a hard substrate. However, the requirement of vacuum system would be a drawback for large area application. And the more intensive works for further improvement of pattern resolution and applications to the device fabrication should be followed.

■ ASSOCIATED CONTENT

ⓢ Supporting Information

Experimental details (with movie clips); real-time movies of selected patterning examples; technical discussions of the AFN printing including NP dispersion, nozzle clogging, printing speed, adhesion, and near-axis/off-axis patterns; derivations of the optimum process window and details on the CFD simulations; movie clips of in situ images taken inside the chamber during excitation and purging; SEM images of the starting NPs; optical microscope imagery and surface profile measurement of the rectangular pattern of BaTiO$_3$ on a Cu-coated Si substrate; the details of the application examples of AFN printing. This material is available free of charge via the Internet at http://pubs.acs.org.

■ AUTHOR INFORMATION

Corresponding Author
*E-mail: ahnsh@snu.ac.kr.

■ REFERENCES

(1) Kim, H.; Kim, J.; Yang, H.; Suh, J.; Kim, T.; Han, B.; Kim, S.; Kim, D. S.; Pikhitsa, P. V.; Choi, M. Parallel Patterning of Nanoparticles via Electrodynamic Focusing of Charged Aerosols. *Nat. Nanotechnol.* **2006**, *1*, 117−121.

(2) Lee, H.; You, S.; Pikhitsa, P. V.; Kim, J.; Kwon, S.; Woo, C. G.; Choi, M. Three-Dimensional Assembly of Nanoparticles from Charged Aerosols. *Nano Lett.* **2011**, *11*, 119−124.

(3) Schirmer, N. C.; Kullmann, C.; Schmid, M. S.; Burg, B. R.; Schwamb, T.; Poulikakos, D. On Ejecting Colloids against Capillarity from Sub-Micrometer Openings: On-Demand Dielectrophoretic Nanoprinting. *Adv. Mater.* **2010**, *22*, 4701−4705.

(4) Zhang, Z.; Zhang, X.; Xin, Z.; Deng, M.; Wen, Y.; Song, Y. Controlled Inkjetting of a Conductive Pattern of Silver Nanoparticles Based on the Coffee-Ring Effect. *Adv. Mater.* **2013**, *25*, 6714−6718.

(5) Zhang, L.; Liu, H.; Zhao, Y.; Sun, X.; Wen, Y.; Guo, Y.; Gao, X.; Di, C. A.; Yu, G.; Liu, Y. Inkjet Printing High-Resolution, Large-Area Graphene Patterns by Coffee-Ring Lithography. *Adv. Mater.* **2011**, *24*, 436−440.

(6) Champagne, V.; Helfritch, D.; Wienhold, E.; DeHaven, J. Deposition of Copper Micro-Circuitry by Capillary Focusing. *J. Micromech. Microeng.* **2013**, *23*, 065023.

(7) Yun, C.; Choi, J.; Kang, H. W.; Kim, M.; Moon, H.; Sung, H. J.; Yoo, S. Digital-Mode Organic Vapor-Jet Printing (D-Ovjp): Advanced Jet-on-Demand Control of Organic Thin-Film Deposition. *Adv. Mater.* **2012**, *24*, 2857−2862.

(8) Mahajan, A.; Frisbie, C. D.; Francis, L. F. Optimization of Aerosol Jet Printing for High Resolution, High Aspect Ratio Silver Lines. *ACS Appl. Mater. Interfaces* **2013**, *5*, 4856−4864.

(9) Park, J. U.; Hardy, M.; Kang, S. J.; Barton, K.; Adair, K.; Mukhopadhyay, D. K.; Lee, C. Y.; Strano, M. S.; Alleyne, A. G.; Georgiadis, J. G.; Ferreira, P. M.; Rogers, J. A. High-Resolution Electrohydrodynamic Jet Printing. *Nat. Mater.* **2007**, *6*, 782−789.

(10) Boissiere, C.; Grosso, D.; Chaumonnot, A.; Nicole, L.; Sanchez, C. Aerosol Route to Functional Nanostructured Inorganic and Hybrid Porous Materials. *Adv. Mater.* **2011**, *23*, 599−623.

(11) Kim, J. Y.; Ingrosso, C.; Fakhfouri, V.; Striccoli, M.; Agostiano, A.; Curri, M. L.; Brugger, J. Inkjet-Printed Multicolor Arrays of Highly Luminescent Nanocrystal-Based Nanocomposites. *Small* **2009**, *5*, 1051−1057.

(12) Shtein, M.; Peumans, P.; Benziger, J. B.; Forrest, S. R. Direct, Mask- and Solvent-Free Printing of Molecular Organic Semi-conductors. *Adv. Mater.* **2004**, *16*, 1615−1620.

(13) Ladj, R.; Bitar, A.; Eissa, M.; Mugnier, Y.; Le Dantec, R.; Fessi, H.; Elaissari, A. Individual Inorganic Nanoparticles: Preparation, Functionalization and in Vitro Biomedical Diagnostic Applications. *J. Mater. Chem. B* **2013**, *1*, 1381−1396.

(14) Chun, D. M.; Ahn, S. H. Deposition Mechanism of Dry Sprayed Ceramic Particles at Room Temperature using a Nano-Particle Deposition System. *Acta Mater.* **2011**, *59*, 2693−2703.

(15) Akedo, J. Room Temperature Impact Consolidation (Rtic) of Fine Ceramic Powder by Aerosol Deposition Method and Applications to Microdevices. *J. Therm. Spray Technol.* **2008**, *17*, 181−198.

(16) Schmidt, T.; Gärtner, F.; Assadi, H.; Kreye, H. Development of a Generalized Parameter Window for Cold Spray Deposition. *Acta Mater.* **2006**, *54*, 729−742.

(17) Huang, C. Supersonic Jet Deposition of Silver Nanoparticle Aerosols: Correlations of Impact Conditions and Film Morphologies. *J. Appl. Phys.* **2007**, *101*, 064902.

(18) Wang, X.; Gidwani, A.; Girshick, S. L.; McMurry, P. H. Aerodynamic Focusing of Nanoparticles: II. Numerical Simulation of Particle Motion through Aerodynamic Lenses. *Aerosol Sci. Technol.* **2005**, *39*, 624−636.

(19) Liu, P.; Ziemann, P. J.; Kittelson, D. B.; McMurry, P. H. Generating Particle Beams of Controlled Dimensions and Divergence: I. Theory of Particle Motion in Aerodynamic Lenses and Nozzle Expansions. *Aerosol Sci. Technol.* **1995**, *22*, 293−313.

(20) Di Fonzo, F.; Gidwani, A.; Fan, M. H.; Neumann, D.; Iordanoglou, D. I.; Heberlein, J. V. R.; McMurry, P. H.; Girshick, S. L.; Tymiak, N.; Gerberich, W. W.; Rao, N. P. Focused Nanoparticle-Beam Deposition of Patterned Microstructures. *Appl. Phys. Lett.* **2000**, *77*, 910−912.

(21) Kim, S. H.; Hong, K.; Lee, K. H.; Frisbie, C. D. Performance and Stability of Aerosol-Jet-Printed Electrolyte-Gated Transistors Based on Poly(3-Hexylthiophene). *ACS Appl. Mater. Interfaces* **2013**, *5*, 6580−6585.

(22) Wang, X.; Kruis, F. E.; McMurry, P. H. Aerodynamic Focusing of Nanoparticles: I. Guidelines for Designing Aerodynamic Lenses for Nanoparticles. *Aerosol Sci. Technol.* **2005**, *39*, 611−623.

(23) Hinds, W. C. *Aerosol Technology: Properties, Behavior, and Measurement of Airborne Particles*; Wiley: New York, 1999.

(24) Nagata, H.; Ko, S. W.; Hong, E.; Randall, C. A.; Trolier-McKinstry, S.; Pinceloup, P.; Skamser, D.; Randall, M.; Tajuddin, A. Microcontact Printed $BaTiO_3$ and $LaNiO_3$ Thin Films for Capacitors. *J. Am. Ceram. Soc.* **2006**, *89*, 2816−2821.

(25) Park, K. I.; Xu, S.; Liu, Y.; Hwang, G. T.; Kang, S. J.; Wang, Z. L.; Lee, K. J. Piezoelectric BaTiO(3) Thin Film Nanogenerator on Plastic Substrates. *Nano Lett.* **2010**, *10*, 4939−4943.

(26) Fernandez de la Mora, J.; Hering, S. V.; Rao, N.; McMurry, P. H. Hypersonic Impaction of Ultrafine Particles. *J. Aerosol Sci.* **1990**, *21*, 169−187.

(27) Akhatov, I. S.; Hoey, J. M.; Swenson, O. F.; Schulz, D. L. Aerosol Focusing in Micro-Capillaries: Theory and Experiment. *J. Aerosol Sci.* **2008**, *39*, 691−709.